Angewandte Chemie International Edition

Angewandte International Edition Chemie

GDCh German Chemical Society

How to cite: *Angew. Chem. Int. Ed.* **2026**, 65, e5543861
doi.org/10.1002/anie.5543861

RESEARCH ARTICLE

A Low-Temperature Solid Chemistry to Ru Clusterrene for Scalable Hydrogen Production

Rui Qin[1,2] | Tongshuai Wang[3,4] | Zhiyong Yu[1] | Zhongliang Huang[1] | Qunyang He[5,6] | Huiping Peng[1] | Qingyu Kong[7] | Jihao Zhang[7] | Shu-Chih Haw[8] | Zhiwei Hu[9] | Linjuan Zhang[3,4] | Nanjun Chen[1,10] | Qing Yao[2] | Xiaoqing Huang[1,10]

[1]State Key Laboratory of Physical Chemistry of Solid Surfaces, College of Chemistry and Chemical Engineering, Xiamen University, Xiamen, China | [2]College of Materials Science and Engineering, Huaqiao University, Xiamen, China | [3]Key Laboratory of Interfacial Physics and Technology, Shanghai Institute of Applied Physics, Chinese Academy of Sciences, Shanghai, China | [4]University of Chinese Academy of Sciences, Beijing, China | [5]Department of Chemical and Biochemical Engineering, College of Chemistry and Chemical Engineering, Xiamen University, Xiamen, China | [6]Reactive Hazards Evaluation Laboratory, Gulei Innovation Institute, Xiamen University, Zhangzhou, China | [7]Synchrotron Soleil, L'Orme Des Merisiers, Gif-sur-Yvette, France | [8]National Synchrotron Radiation Research Center, Hsinchu, Taiwan | [9]Max Planck Institute for Chemical Physics of Solids, Dresden, Germany | [10]Innovation Laboratory for Sciences and Technologies of Energy Materials of Fujian Province (IKKEM), Xiamen, China

Correspondence: Qing Yao (yq13456245617@163.com) | Xiaoqing Huang (hxq006@xmu.edu.cn)

Received: 2 December 2025 | **Revised:** 24 March 2026 | **Accepted:** 30 March 2026

Keywords: anion exchange membrane water electrolysis| low-temperature calcination| Ru clusterrene| stack performance| thermal buffer

ABSTRACT

Platinum-group-metal (PGM) nanomaterials are prominent in chemical and energy conversions. To date, their scalable manufacturing is confined by complex post-processing or high-temperature calcination (≥ 800°C), which are often required for conventional small-sized nanoparticles. Herein, we have successfully developed a thermal buffer-assisted low-temperature (250°C) calcination strategy to create a sub-nano Ru metallene called "Ru clusterrene" for anion exchange membrane water electrolysis (AEMWE). The rational use of NaCl is pivotal for successful synthesis, serving as a "buffer" to prevent thermal runaway. Consequently, the Ru clusterrene exhibits an ultra-thin, fluid-like structure that enables strong interaction with the substrate and ensures maximized active site exposure. Importantly, this strategy costs only US$39.42/$g_{Ru}$, which is substantially lower than that of commercial Ru/C (Premetek, US$1407.50/$g_{Ru}$). The Ru clusterrene delivers an outstanding activity of 1.73 V@2 A cm^{-2} and 2.0 V@5.4 A cm^{-2}, as well as an unprecedented stability for 1000 h at 2 A cm^{-2} (80°C) and 3500 h at 1 A cm^{-2} (50°C). More significantly, it exhibits a high stack performance in AEMWE (3.6 V@1 A cm^{-2} and 2000 h@25 A), representing the most advanced level for AEMWE cathode catalyst.

1 | Introduction

Anion exchange membrane water electrolysis (AEMWE) is widely considered as a promising technique for green hydrogen production, offering advantages such as high energy conversion efficiency, high hydrogen purity, and a wide range of available electrode materials. Nevertheless, the practical implementation of AEMWE is still impeded by sluggish reaction kinetics and unsatisfactory long-term stability under high current density conditions [1, 2]. Therefore, it is imperative to develop highly efficient and facilely prepared electrocatalysts for accelerating the advancement of AEMWE. Among various catalyst candidates, platinum-group-metal (PGM)-based nanomaterials serve as promising alternatives for enhancing catalytic performance

Rui Qin and Tongshuai Wang contributed equally to this work.

of AEMWE systems. This potential stems from their favorable adsorption energy for reaction intermediates and improved degradation resistance [3–6]. Various attentions have mainly focused on developing PGM-based electrocatalysts, particularly emphasizing nanostructured configurations such as small-sized nanoparticles [7]. These nanostructures exhibit enhanced catalytic performance in AEMWE applications due to their high surface area, abundant edge sites, and the shortened diffusion path, enabling high activity with improved energy efficiency [8, 9]. Nevertheless, further performance breakthroughs for small-sized catalysts are constrained by their inherently high surface energy and weak interactions with the substrate, which often lead to nanoparticle agglomeration and Ostwald ripening during prolonged electrocatalysis, especially under industrial current densities [10–13].

The methodologies employed in catalyst preparation are critical to both scalable production and catalytic performance. The ligand-mediated strategy, typically based on liquid-phase methods, is a predominant approach for fabricating small-sized catalysts, enabling precise control over the size and morphology of PGM-based nanomaterials by flexibly tuning the ligands [14–19]. However, the catalysts prepared by this method invariably require post-processing before electrochemical applications, including loading onto conductive support and complex procedures to eliminate the surface-coated organic impurities [20–22]. These technical complexities largely hamper many advanced catalysts in large-scale applications. Alternatively, direct calcination methods have attracted growing interest due to their operational simplicity and scalability in preparing small-sized catalysts. This thermal process typically relies on extreme temperature ($\geq 800°C$) to anchor small-sized nanoparticles and achieve favorable phase or composition [23–25]. Regrettably, such high-temperature calcination invariably triggers morphology change and severe sintering of PGM-based catalysts, undermining the intrinsic merits of this methodology and presenting substantial challenges for mass production of high-performance catalysts [26]. Consequently, to enable the industrial-scale AEMWE, low-temperature calcination strategies must be developed to create small-sized PGM-based catalysts simultaneously with favorable morphology and structural stability.

Herein, we report a thermal buffer-assisted strategy based on low-temperature (250°C) solid chemistry to synthesize a sub-nano Ru clusterrene as a highly active and durable catalyst for AEMWE. This nanostructure maintains the initial condensed matter state with a low-ordered atomic arrangement and low crystallization. Meanwhile, this configuration is analogous to an ultrathin graphene-like layer which is distributed and firmly anchored onto the carbon support, ensuring exceptional structural integrity without compromising its inherent catalytic activity. Mechanism studies demonstrate that the introduced NaCl acts as a thermal buffer for thermodynamic control, providing homogeneous heat flow during the nucleation and growth of Ru. This scalable synthesis achieves a single-batch yield of 15.19 g of catalysts at a cost of merely US\$39.42/g_{Ru}. More significantly, the Ru clusterrene-based AEMWE delivers an excellent activity of 1.73 V@2 A cm^{-2}, surpassing most reported small-sized catalysts and exceeding the multi-year program plan proposed by the United States Department of Energy (DOE). We also demonstrate, for the first time, this clusterrene can run stably for 1000 h at 2 A cm^{-2} without decay. Moreover, it achieves extended durability for 3500 h at 50°C. To evaluate its potential in practical application, a two-cell stack of AEMWE is constructed, which exhibits a high performance of 3.6 V at 1 A cm^{-2}. Under a constant current of 25 A, the stack maintains stable operation for 2000 h, representing an unprecedented level for cathodic catalysts in AEMWE.

2 | Results and Discussion

Ru clusterrene was synthesized by a simple yet efficient low-temperature (250°C) calcination strategy with the assistance of NaCl (Figure S1). By this strategy, Ru atoms migrate disorderedly and self-assemble into graphene-like layers on the carbon substrate, exhibiting irregular fluid-shape devoid of close-packed order (Figure 1a) [27]. The fluid behavior is mainly attributed to the molten state of the $Ru(acac)_3$, which allows the Ru precursor to grow along the curved surface of carbon, driving the formation of thin layers. The Ru loading is close to the theoretical value, as revealed by the thermogravimetry (TG) analysis (Figure S2). In contrast, in the absence of NaCl, Ru atoms readily coalesce and agglomerate into large particles. As depicted in bright-field scanning transmission electron microscope (BF-STEM) images, no discernible nanoparticles are found on the surface of carbon support (Figure S3). However, high-angle annular dark-field STEM (HAADF-STEM) images clearly reveal the presence of ultrathin graphene-like layers with fluid-like morphology distributed on the carbon support (Figure 1b,c). These spread layers correspond to Ru species, as confirmed by HAADF-STEM energy-dispersive spectroscopy (EDS) elemental mapping analysis (Figure S4). As further visualized in pseudo-color-enhanced HAADF-STEM images, the green areas that correspond to the Ru clusterrene exhibit low contrast and nonequilibrium geometrical shape, spreading across the carbon surface (Figures 1d and S5). In sharp contrast, completely different products consisting of obvious Ru nanoparticles are obtained from the NaCl-free system (Figures S6 and S7). These nanoparticles are stacked with each other, resulting in obvious bright areas in the pseudo-color image (Figure 1e–g). Consistently, Ru clusterrene shows weak crystallinity in the X-ray diffraction (XRD) pattern (Figure S8), whereas the Ru nanoparticle has a series of sharp peaks corresponding to Ru (PDF#06–0663) and RuO_2 (PDF#43–1027). In the terms "Ru clusterene" and "Ru nanoparticle", "Ru" denotes the overall Ru-based composition, which consists of metallic Ru and RuO_2.

To further reveal the unique structure of this newly developed "clusterrene", a spherical aberration-corrected transmission electron microscope (AC-TEM) was employed. As illustrated in the AC-BF-STEM images (Figures 2a and S9), the thickness of Ru clusterrene is less than 1 nm, corresponding to approximately 5 atomic layers. Notably, the contact angle between these layers and the carbon surface is about 30°. This wetting behavior indicates that the clusterrene is overspread on the substrate, thereby generating abundant interfacial reaction sites. Moreover, the close contact also indicates a strong metal-support interaction (MSI) [12, 28]. The particle-stacked morphology observed in the control sample without carbon substrate further confirms the significant role of MSI in the clusterrene (Figure S10). Oppositely, the Ru nanoparticle exhibits contact angles exceeding 100°,

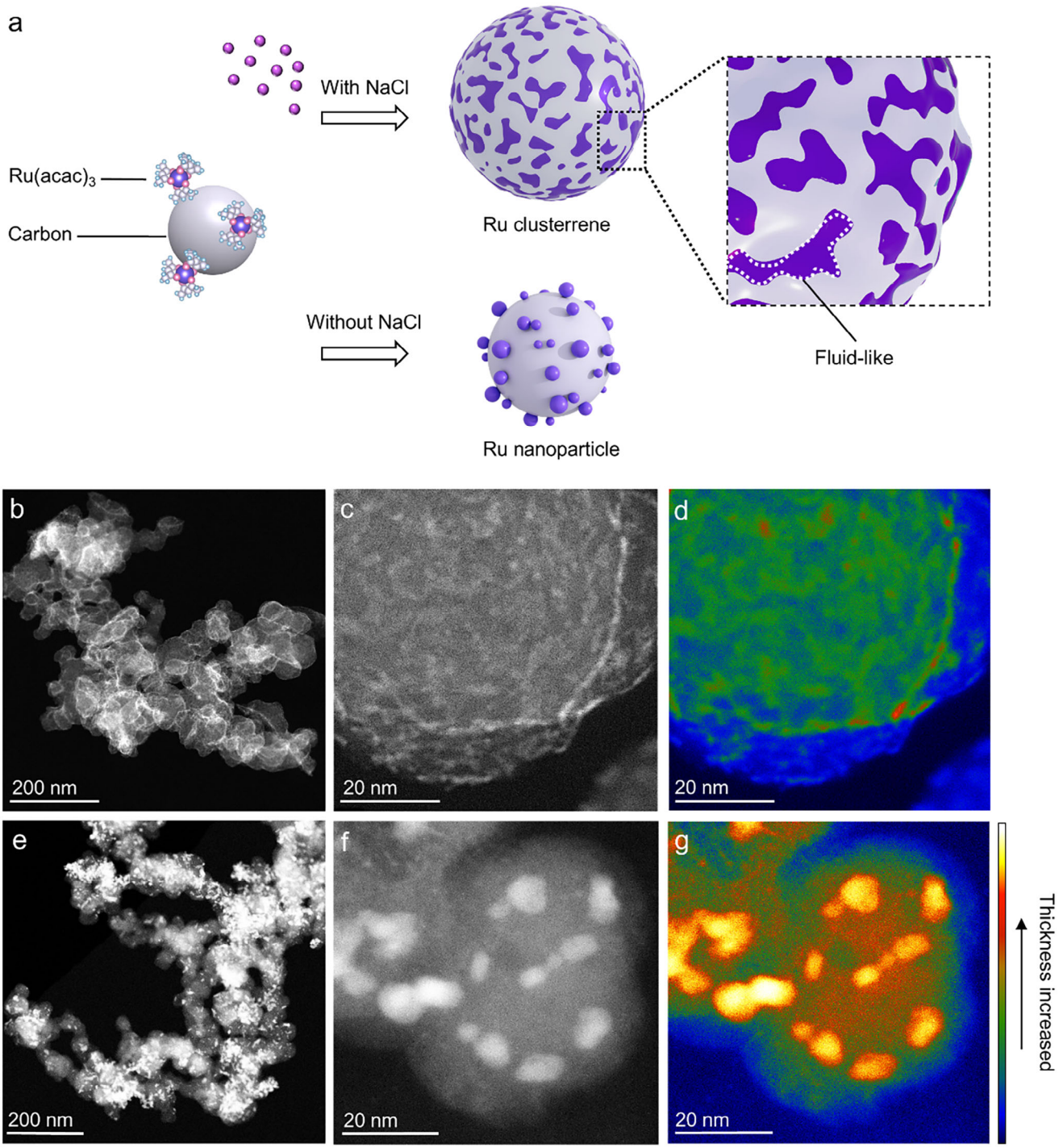

FIGURE 1 | (a) Schematic illustration of "buffer-assisted" strategy. HAADF-STEM images of (b, c) Ru clusterrene and (e, f) Ru nanoparticle. Pseudocolor-enhanced HAADF-STEM images of (d) Ru clusterrene and (g) Ru nanoparticle.

analogous to a hydrophobic surface with limited connected sites (Figure S11), demonstrating a weak interfacial connectivity. AC-HAADF-STEM images reveal that individual cluster units of Ru clusterrene, ranging from 1 to 3 nm, interconnect to form continuous domains, a feature that markedly differs from conventional isolated clusters (Figures 2b and S12). Furthermore, most Ru atoms are arranged randomly within clusterrene, suggesting that the MSI surpasses the cohesive energy of atoms. When atoms adopt a regular arrangement, a nanosheet morphology with continuous lattice fringes characteristic of close-packed Ru is formed (Figure S13). Moreover, the crystal structure of Ru nanoparticle is easily detected by high-resolution TEM (HRTEM), with measured lattice spacings corresponding to RuO_2 (101), Ru (100), and Ru (002) (Figure S14).

The unconventional morphology and crystal structure suggest a unique electronic structure and coordination environment of Ru atoms in the clusterrene. The X-ray absorption near-edge structure (XANES) spectrum of Ru K-edge in the clusterrene exhibits an average valence between that in Ru foil and RuO_2,

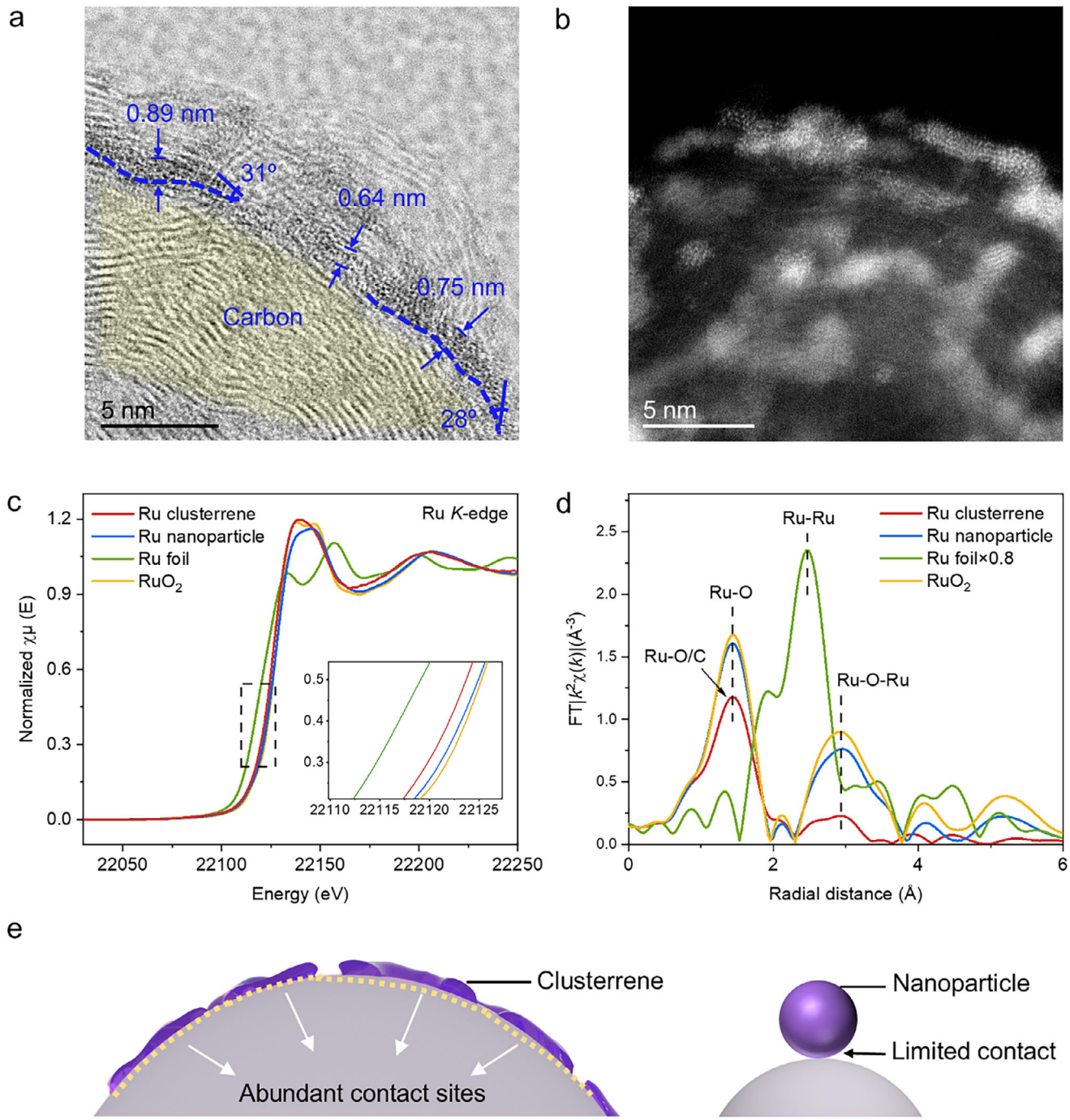

FIGURE 2 | (a) AC-BF-STEM image and (b) AC-HAADF-STEM image of Ru clusterrene. (c) Ru K-edge XANES and (d) FT-EXAFS spectra of Ru clusterrene, Ru nanoparticle, Ru foil, and RuO_2. (e) Schematic of the cross-section in Ru clusterrene and Ru nanoparticle.

and is lower than that in the nanoparticle (Figure 2c). Furthermore, the Fourier-transformed extended X-ray absorption fine structure (FT-EXAFS) spectra reveal the different coordination environments of Ru atom in the Ru clusterrene and RuO_2 (Figure 2d) [29]. These features indicate that the crystal structure of Ru clusterrene is not fully consistent with that of crystalline RuO_2, distinguishing it from the Ru nanoparticle. The partially oxidized chemical state of Ru clusterrene mainly stems from the strong interaction between clusterrene and carbon, which provides a stable interface that prevents self-nucleation of Ru atoms during synthesis and suppresses serious aggregation of Ru clusterrene during catalysis. Wavelet transform (WT) analysis further supports the above findings. The intensity of Ru clusterrene at ~4 $Å^{-1}$ is attributed to Ru—O/C bonds. This intensity is lower than that in completely oxidized Ru in Ru nanoparticle and RuO_2 (Figure S15). The presence of Ru—C suggests chemisorption at the interface, contributing to the strong adhesion. Additionally, fitting results show that the coordination number of Ru—O within the first shell in Ru clusterrene (4.84) is lower than that in Ru nanoparticle (5.04) (Figures S16–S18 and Table S1), indicating more unsaturated sites exposed on the clusterrene surface, which is beneficial for high catalytic activity. A similar trend is observed

in O 1s X-ray photoelectron spectroscopy (XPS) spectra, where the lattice oxygen signal in Ru clusterrene is significantly weaker than that in Ru nanoparticle (Figure S19). Moreover, this Ru—O signal (530.1 eV) shifts toward higher binding energy compared to that of Ru nanoparticle (529.4 eV) and highly crystalline RuO_2 (529.4 eV), indicating strong electron transfer between Ru clusterrene and substrate. These structural differences result in abundant contact sites at the interface for Ru clusterrene, in contrast to limited sites for Ru nanoparticle (Figure 2e).

To elucidate the mechanism of Ru clusterrene, systematic investigations were performed. TG analysis demonstrates that the weight loss of the precursor powder terminates before 250°C (Figure S20), indicating the ligand removal from the Ru precursor predominantly occurs before 250°C. Significantly, simulated infrared thermography analysis unveils a distinct thermal effect between Ru clusterrene and Ru nanoparticle during the calcination (Figure 3a–d). In the ligand-removal window (200°C–250°C), the NaCl-containing precursors of Ru clusterrene exhibit a markedly lower temperature increase rate compared to that of NaCl-free powder of Ru nanoparticle (1.14 vs. 2.28°C/s). Moreover, as the simulation program progresses, the temperature of Ru clusterrene remains constant with the assistance of NaCl. However, the Ru nanoparticle experiences a thermal runaway, which subsequently results in vigorous combustion (Movies S1 and S2). The heat flow during calcination is collected by the differential scanning calorimetry (DSC) in a synchronous thermal analyzer (Figure S21), revealing that the heat released from the clusterrene is 60.6 J g^{-1}, sixfold lower than that from the nanoparticle (413.8 J g^{-1}).

Mass spectra (MS) analysis of the released products during calcination reveals the distinct signals of C ($m/z = 12$) and CO_2 ($m/z = 44$) (Figure 3e,f). These signals correspond to the pyrolysis and oxidation of acetylacetone ligands in the Ru precursor, respectively, as evidenced by the control experiments excluding contributions from the carbon substrate (Figures S22 and S23). More importantly, the significantly lower CO_2/C ratio for Ru clusterrene compared to that for Ru nanoparticle (30 vs. 600) further verifies the more controllable thermal process facilitated by NaCl. Moreover, an extra peak belonging to -CH_2- or C—O group in Ru clusterrene is notably stronger than that in Ru nanoparticle, as detected by the surface sensitive total electron yield (TEY) pattern of soft X-ray absorption spectroscopy (sXAS) at C *K*-edge (Figure 3g), which is consistent with the above observations [30, 31]. Benefiting from the moderate heat distribution, the strong MSI is well preserved. Consequently, Ru clusterrene maintains the fluid-like morphology and initial cluster size after the heat insulation process (Figures 3h and S24). In contrast, Ru nanoparticle undergoes agglomeration with notable particle growth and phase evolution under the same calcination procedure (Figure S25).

With the melting point substantially exceeding the calcination temperature, NaCl acts as a thermal buffer by absorbing substantial heat, thereby providing a homogeneous thermal environment for nucleation and growth of Ru clusterrene during calcination. The underlying mechanism involves NaCl initially absorbing partial heat supplied by the muffle supply, leading to insufficient energy for all acetylacetone groups to break their chemical bonding. Consequently, the ligands undergo partial pyrolysis or mild oxidation, and then the released heat is absorbed again by NaCl. The mild thermal environment allows clusterrene to constantly interact with the substrate, leading to strong adhesion. In contrast, in the absence of such a thermal buffer, the NaCl-free system allows heat to flow randomly among Ru atoms, resulting in uncontrolled thermal feedback (Figures 3i and S26). This thermal instability leads to the heterogeneity in both particle size and distribution of Ru nanoparticle. Notably, a similar thermal buffer effect also appears in other sodium halides and alkali chlorides (e.g., NaBr, NaI, LiCl, and KCl) (Figure S27), all of which promote a homogeneous growth environment for Ru atoms.

The hydrogen evolution reaction (HER) performance of Ru clusterrene was first evaluated using a three-electrode system in 1 M KOH electrolyte. The polarization curves show that Ru clusterrene exhibits the highest HER activity, with overpotentials of only 12 and 48 mV to reach current densities of 10 and 100 mA cm^{-2}, respectively (Figure 4a). These values are significantly superior to those of Ru nanoparticle (83 and 188 mV), commercial Ru/C (28 and 143 mV), and commercial Pt/C (28 and 138 mV), even surpassing most state-of-the-art catalysts (Table S2). The lowest Tafel slope of 56.5 mV dec^{-1} further reveals this superior HER kinetics (Figure S28). The electrochemical surface area (ECSA) was evaluated via the double-layer capacitance (C_{dl}). CV curves in the non-faradic region showcase a higher C_{dl} value of Ru clusterrene (20.6 mF cm^{-2}) than that of Ru nanoparticle (14.2 mF cm^{-2}) and commercial Pt/C (15.1 mF cm^{-2}) (Figure S29), demonstrating that more active sites are exposed in the Ru clusterrene. Moreover, mass activity of Ru clusterrene reaches 1.29 and 3.03 A mg^{-1} at the overpotential of 50 and 100 mV, respectively, which are 32-fold and 13-fold those of Ru nanoparticle, indicating its superior atomic utilization efficiency (Figure S30). The turnover frequency (TOF) was calculated to compare the H_2 conversion efficiency (Figure S31). At an overpotential of 50 mV, the Ru clusterrene achieves the highest TOF value of 9.08 H_2 s^{-1}, surpassing the Ru nanoparticle (0.50 H_2 s^{-1}) and commercial Pt/C (5.95 H_2 s^{-1}). This enhanced TOF value is attributed to the fast electron dynamics during HER. The strong MSI facilitates the electron redistribution of Ru species and thus optimizes the intermediates adsorption on their surface. These behaviors endow the Ru clusterrene with a lower charge transfer resistance, as indicated by a smaller semi-circular diameter in the Nyquist plot (Figure S32). The above results exhibit the effectiveness of our thermal-buffer strategy in facilitating the HER activity. Moreover, this active Ru clusterrene also exhibits excellent stability, with negligible decay after operating at 100 mA cm^{-2} up to 250 h (Figure S33). The superior electrocatalytic performance of Ru clusterrene over Ru nanoparticle highlights the crucial role of its unique structure and the resulting strong MSI.

Most significantly, the AEMWE employing Ru clusterrene as the cathode catalyst shows substantially enhanced performance (Figure S34). As evidenced by the current-voltage curves, Ru clusterrene attains the lowest recorded cell voltage of 1.63 V at 1 A cm^{-2} among the recently reported AEMWE (Figure 4b and Table S3). Moreover, it requires merely 1.73 V to achieve an elevated current density of 2 A cm^{-2}, outperforming both Ru nanoparticle (1.86 V@2 A cm^{-2}) and commercial Pt/C (1.78 V@2 A cm^{-2}), while also exceeding the DOE benchmark (1.80 V@2 A cm^{-2}). Significantly, Ru clusterrene enables an ultra-high current density of 7 A cm^{-2} with a low cell voltage of 2.11 V, whereas Ru nanoparticle and

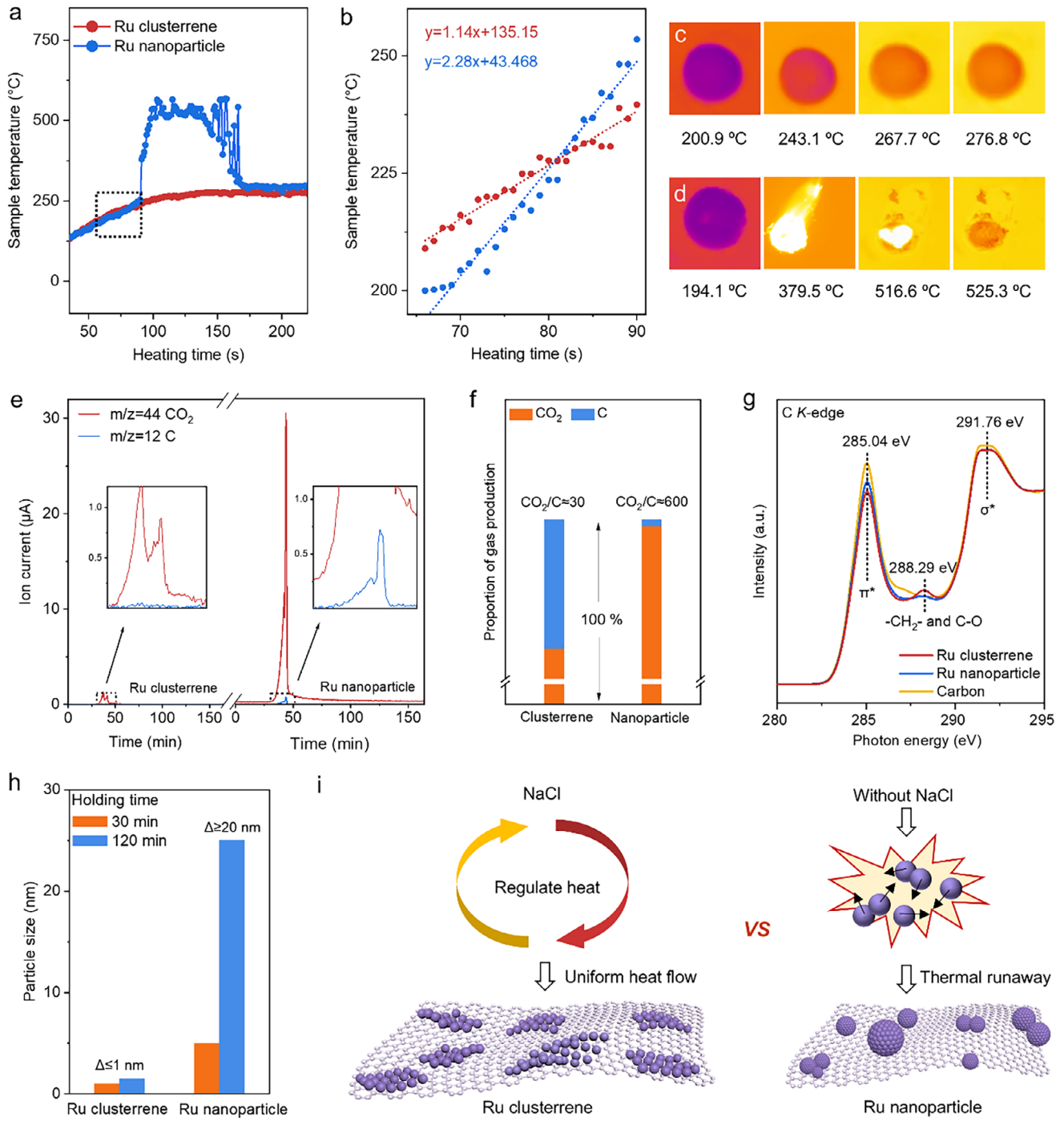

FIGURE 3 | (a) Temperature evolution of the precursor powder during thermal process. (b) Magnification of the black dotted frame in (a). The infrared thermograph images of (c) Ru clusterrene and (d) Ru nanoparticle during thermal process in (a). (e) MS results of Ru clusterrene and Ru nanoparticle. Insets: the magnification of the dotted frame. (f) The ratio of CO_2 to C in (e). (g) TEY mode of C *K*-edge sXAS spectra for Ru clusterrene, Ru nanoparticle, and carbon. (h) Particle size change of Ru clusterrene and Ru nanoparticle after varied insulation times. (i) Schematic illustration of thermal effect in the synthesis process of Ru clusterrene and Ru nanoparticle.

commercial Pt/C need substantially higher voltages to drive this ampere-scale water electrolysis. The durability of Ru-clusterrene-based AEMWE was systematically assessed through continuous hydrogen production under different current densities (1, 2, 3, and 4 A cm^{-2}) (Figure 4c). These cells demonstrate an ability to maintain their initial voltage during long-time testing. Notably, the clusterrene-based AEMWE can run stably at 2 A cm^{-2} for 1000 h without obvious cell voltage decay. After the durability test, Ru clusterrene exhibits no significant size growth, suggesting that severe agglomeration is effectively prevented (Figure S35). Additionally, the surface chemical environment of Ru is well-preserved after long-term operation (Figure S36), further confirming the structural stability of this catalyst. The stability performance is unprecedented among reported cutting-edge cathode catalysts (Figure 4d). In contrast, Ru nanoparticle-based system is difficult to withstand such high current density and

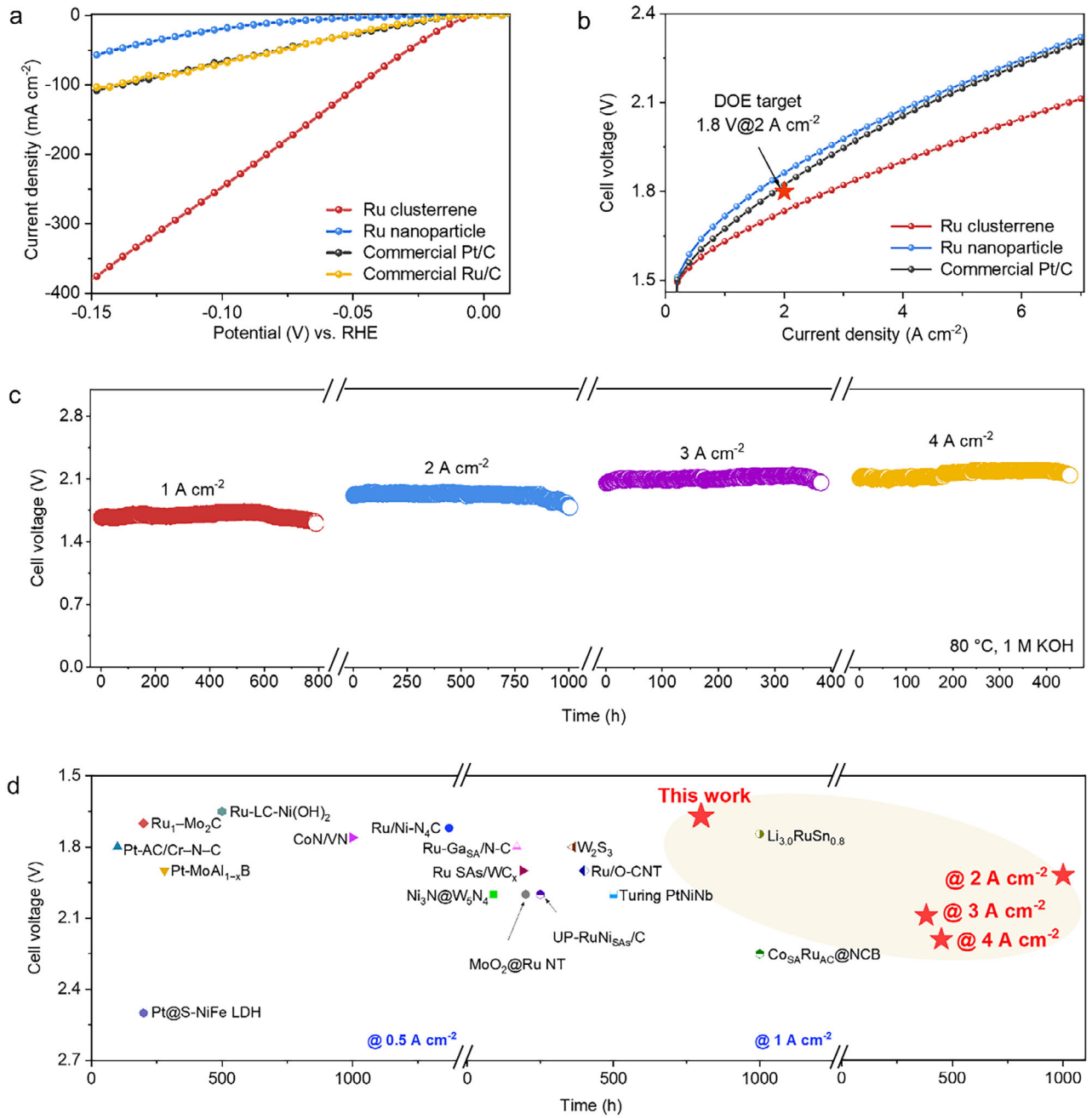

FIGURE 4 | (a) HER polarization curves of Ru clusterrene, Ru nanoparticle, commercial Pt/C, and commercial Ru/C. (b) *I–V* curves of a 1-cm^2 MEA based on different cathodes: Ru clusterrene, Ru nanoparticle, and commercial Pt/C. (c) Voltage–time curves of Ru clusterrene at different current densities. Each current density was measured with a fresh sample. (d) Stability comparison of Ru clusterrene with recently reported cathodes.

breaks down before reaching an operating time of 200 h (Figure S37). These results demonstrate the outstanding potential of Ru clusterrene as a cathode catalyst for AEMWE.

More significantly, the low-temperature synthesis procedure reported herein enables the scalable production of high-performance Ru clusterrene (see method details in Supporting Information). A single batch can yield up to 15.19 g of catalyst (Figures 5a and S38), with production costs of only US\$9.83/$g_{catalyst}$ and US\$39.42/g_{Ru} (Figure S39). These values are substantially lower than the state-of-the-art commercial catalysts, such as Pt/C (e.g., TANAKA, 20 wt%, US\$394.40/g_{Pt}), Ru/C (e.g., Premetek, 20 wt%, US\$1407.50/g_{Ru}), and PtRu/C (e.g., Premetek, 40 wt%, US\$411.10/g_{Pt+Ru}), significantly cutting the cost for synthesizing high-performance noble metal catalysts (Figure 5b and Table S4). Remarkably, the scaled-up production preserves the structural and performance consistency with laboratory-scale synthesis (Figure S40). The scaled-up products also exhibit commendable stability in AEMWE at different temperatures, especially maintaining continuous operation for 3500 h at 50°C (Figure 5c). Finally, a two-cell stack (100 W) was constructed to further identify the potential of Ru clusterrene in industrial applications (Figures 5d and S41). It can be seen that the clusterrene exhibited a high stack performance of 3.6 V at 1 A cm^{-2} (Figure 5e). The voltage of stack shows no significant increase for 2000-h operation under ultra-high current of 25 A

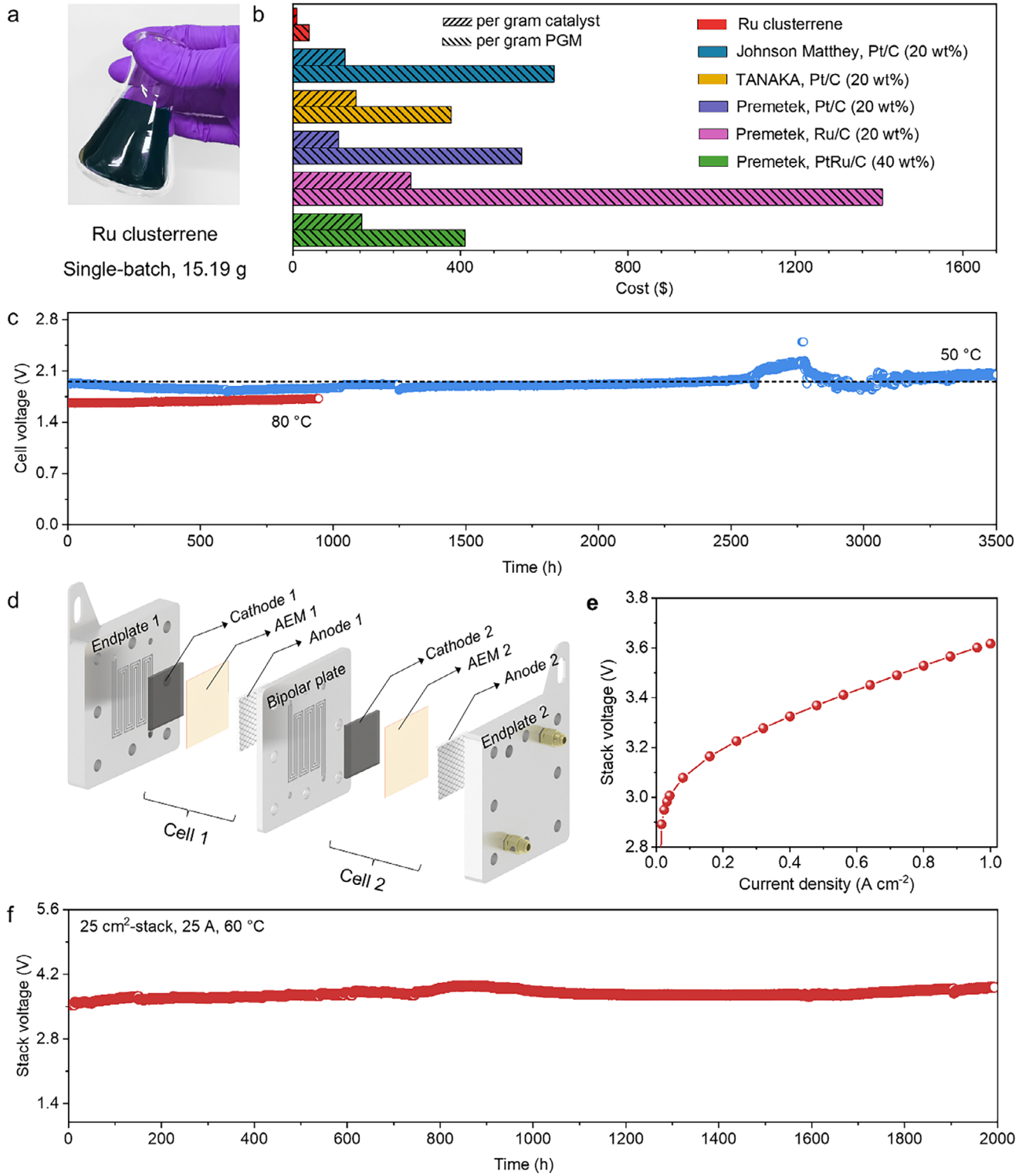

FIGURE 5 | (a) Optical image of scaled-up products for Ru clusterrene. (b) Cost comparison of Ru clusterrene with commercial PGM catalysts. (c) Stability test at different temperatures of scaled-up products for Ru clusterrene in the single-cell AEMWE. Discontinuities in the plot correspond to power shutdown/startup or electrolyte replenishment. (d) Schematic illustration of AEMWE stack. (e) *I–V* curve of a 25-cm^2 stack for Ru clusterrene. (f) Stability test in AEMWE stack.

(Figure 5f). This level of performance has not been previously reported for AEMWE, suggesting significant progress in both designed synthesis and application of clusterrene-based catalysts. This unprecedented performance underscores the transformative potential of Ru clusterrene and positions the clusterrene as a competitive candidate in the hydrogen economy.

3 | Conclusion

In conclusion, we have proposed a thermal buffer-assisted calcination strategy for cost-effective synthesis of Ru clusterrene. The innovative design differs from conventional carbon-supported catalysts preparation by eliminating the pickling process or other intricate steps. This streamlined protocol provides scalable production of the clusterrene, with a single-batch yield of 15.19 g at a remarkably low cost of US$39.42/$g_{Ru}$, much more economical than state-of-the-art commercial PGM catalysts. Eco-friendly NaCl acts as the buffer to precisely regulate the thermodynamics during calcination, ensuring homogeneous nucleation and controllable growth of clusterrene. The resultant catalyst exhibits a small size (1–3 nm) and atomic thickness (≤ 1 nm), collectively endowing it with exceptional activity and atomic utilization efficiency. The Ru clusterrene achieves DOE-compliant performance in AEMWE, maintaining a current density of 2 A cm^{-2} at 1.73 V with stable operation for 1000 h. More importantly, it also exhibits a high stack performance of 3.6 V at 1 A cm^{-2} and an unprecedented stability for 2000 h. The combination of economic synthesis, distinctive topology, and superlative catalytic performance positions the Ru clusterrene as a transformative competitor in the burgeoning hydrogen energy market.

Acknowledgments

This work was financially supported by the National Key R&D Program of China (2024YFA1509500, 2022YFA1504500), the National Natural Science Foundation of China (22025108, U21A20327, 22121001, 22405224, and 22475181), the Science and Technology Planning Project of Fujian Province of China (2024H0001), the Fundamental Research Funds for the Central Universities (20720240059 and 20720240053), Natural Science Foundation of Xiamen, China (3502Z202473002), the Postdoctoral Fellowship Program of CPSF (GZC20240895), and Start-up supports from Xiamen University. We acknowledge support from the Max Planck-POSTECH-Hsinchu Center for Complex Phase Materials.

Author Contributions

Rui Qin: conceptualization. **Tongshuai Wang:** methodology. **Zhiyong Yu:** methodology. **Zhongliang Huang:** methodology. **Qunyang He:** methodology. **Huiping Peng:** methodology. **Qingyu Kong:** methodology. **Jihao Zhang:** methodology. **Shu-Chih Haw:** methodology. **Zhiwei Hu:** methodology. **Linjuan Zhang:** methodology. **Nanjun Chen:** methodology. **Qing Yao:** conceptualization. **Xiaoqing Huang:** conceptualization.

Conflicts of Interest

The authors declare no conflicts of interest.

Data Availability Statement

The Data That Supports the Findings of this Study Are Available in the Supporting Information of this Article.

References

1. N. Du, C. Roy, R. Peach, M. Turnbull, S. Thiele, and C. Bock, "Anion-Exchange Membrane Water Electrolyzers," *Chemical Reviews* 122 (2022): 11830–11895, https://doi.org/10.1021/acs.chemrev.1c00854.

2. Y. Yang, P. Li, X. Zheng, et al., "Anion-Exchange Membrane Water Electrolyzers and Fuel Cells," *Chemical Society Reviews* 51 (2022): 9620–9693, https://doi.org/10.1039/D2CS00038E.

3. B. Hammer and J. K. Norskov, "Why Gold Is the Noblest of all the Metals," *Nature* 376 (1995): 238–240, https://doi.org/10.1038/376238a0.

4. J. K. Nørskov, T. Bligaard, A. Logadottir, et al., "Universality in Heterogeneous Catalysis," *Journal of Catalysis* 209 (2002): 275–278, https://doi.org/10.1006/jcat.2002.3615.

5. B. Hammer and J. K. Nørskov, "Electronic Factors Determining the Reactivity of Metal Surfaces," *Surface Science* 343 (1995): 211–220, https://doi.org/10.1016/0039-6028(96)80007-0.

6. F. H. B. Lima, J. Zhang, M. H. Shao, et al., "Catalytic Activity–D-Band Center Correlation for the O_2 Reduction Reaction on Platinum in Alkaline Solutions," *Journal of Physical Chemistry C* 111 (2007): 404–410, https://doi.org/10.1021/jp065181r.

7. C. Dong, Z. Gao, Y. Li, et al., "Fully Exposed Palladium Cluster Catalysts Enable Hydrogen Production From Nitrogen Heterocycles," *Nature Catalysis* 5 (2022): 485–493, https://doi.org/10.1038/s41929-022-00769-4.

8. T. Wu, M.-Y. Han, and Z. J. Xu, "Size Effects of Electrocatalysts: More than a Variation of Surface Area," *ACS Nano* 16 (2022): 8531–8539, https://doi.org/10.1021/acsnano.2c04603.

9. H. Cai, H. Yang, S. He, et al., "Size-Adjustable High-Entropy Alloy Nanoparticles as an Efficient Platform for Electrocatalysis," *Angewandte Chemie International Edition* 64 (2025): e202423765, https://doi.org/10.1002/anie.202423765.

10. T. Zhou, X. Li, J. Zhao, et al., "Ultrafine Metal Nanoparticles Isolated on Oxide Nano-Islands as Exceptional Sintering-Resistant Catalysts," *Nature Materials* 24 (2025): 891–899, https://doi.org/10.1038/s41563-025-02134-9.

11. S. Zhang, Y. Han, X.-Y. Li, Q. Tang, B. Zhu, and Y. Gao, "Particle Hopping and Coalescence of Supported Au Nanoparticles in Harsh Reactive Environments," *Journal of the American Chemical Society* 147 (2025): 15796–15805, https://doi.org/10.1021/jacs.5c03633.

12. S. Hu and W.-X. Li, "Sabatier Principle of Metal-Support Interaction for Design of Ultrastable Metal Nanocatalysts," *Science* 374 (2021): 1360–1365, https://doi.org/10.1126/science.abi9828.

13. P. Yin, S. Hu, K. Qian, et al., "Quantification of Critical Particle Distance for Mitigating Catalyst Sintering," *Nature Communications* 12 (2021): 4865, https://doi.org/10.1038/s41467-021-25116-2.

14. Q. Hao, H.-X. Zhong, J.-Z. Wang, et al., "Nickel Dual-Atom Sites for Electrochemical Carbon Dioxide Reduction," *Nature Synthesis* 1 (2022): 719–728, https://doi.org/10.1038/s44160-022-00138-w.

15. M. Zhao and Y. Xia, "Crystal-Phase and Surface-Structure Engineering of Ruthenium Nanocrystals," *Nature Reviews Materials* 5 (2020): 440–459, https://doi.org/10.1038/s41578-020-0183-3.

16. T.-H. Yang, S. Zhou, M. Zhao, and Y. Xia, "Quantitative Analysis of the Multiple Roles Played by Halide Ions in Controlling the Growth Patterns of Palladium Nanocrystals," *ChemNanoMat* 6 (2020): 576–588, https://doi.org/10.1002/cnma.202000049.

17. X. Wang, L. Zhao, X. Li, et al., "Atomic-Precision Pt6 Nanoclusters for Enhanced Hydrogen Electro-Oxidation," *Nature Communications* 13 (2022): 1596, https://doi.org/10.1038/s41467-022-29276-7.

18. Q. Yao, L. Liu, S. Malola, et al., "Supercrystal Engineering of Atomically Precise Gold Nanoparticles Promoted by Surface Dynamics," *Nature Chemistry* 15 (2023): 230–239, https://doi.org/10.1038/s41557-022-01079-9.

19. Y. Zhai, J. S. DuChene, Y.-C. Wang, et al., "Polyvinylpyrrolidone-Induced Anisotropic Growth of Gold Nanoprisms in Plasmon-Driven

Synthesis," *Nature Materials* 15 (2016): 889–895, https://doi.org/10.1038/nmat4683.

20. Y. Zhang, S. Han, S. Zhu, et al., "Slowly Removing Surface Ligand by Aging Enhances the Stability of Pd Nanosheets Toward Electron Beam Irradiation and Electrocatalysis," *Angewandte Chemie International Edition* 62 (2023): e202314634, https://doi.org/10.1002/anie.202314634.

21. J. A. Lopez-Sanchez, N. Dimitratos, C. Hammond, et al., "Facile Removal of Stabilizer-Ligands From Supported Gold Nanoparticles," *Nature Chemistry* 3 (2011): 551–556, https://doi.org/10.1038/nchem.1066.

22. P. Godbold, G. Johnson, A. D. Obi, et al., "Surfactant Removal for Colloidal Nanocrystal Catalysts Mediated by N-Heterocyclic Carbenes," *Journal of the American Chemical Society* 143 (2021): 2644–2648, https://doi.org/10.1021/jacs.0c12278.

23. C.-L. Yang, L.-N. Wang, P. Yin, et al., "Sulfur-Anchoring Synthesis of Platinum Intermetallic Nanoparticle Catalysts for Fuel Cells," *Science* 374 (2021): 459–464, https://doi.org/10.1126/science.abj9980.

24. H. Lei, N. Zhang, S. Hu, et al., "Thermally Triggered Redox Flexibility of Pt/CeO_2 Cluster Catalyst Against In-Situ Atomic Redispersion," *Angewandte Chemie International Edition* 64 (2025): e202509239, https://doi.org/10.1002/anie.202509239.

25. Y. Song, T. Liu, W. Feng, et al., "Atomically Dispersed Ru Species Induced by Strong Metal–Support Interaction for Electrochemical Methane Reforming," *Journal of the American Chemical Society* 146 (2024): 31825–31835, https://doi.org/10.1021/jacs.4c10729.

26. Z. Lyu, R. Chen, M. Mavrikakis, and Y. Xia, "Physical Transformations of Noble-Metal Nanocrystals Upon Thermal Activation," *Accounts of Chemical Research* 54 (2021): 1–10, https://doi.org/10.1021/acs.accounts.0c00640.

27. S. Kashiwaya, Y. Shi, J. Lu, et al., "Synthesis of Goldene Comprising Single-Atom Layer Gold," *Nature Synthesis* 3 (2024): 744–751, https://doi.org/10.1038/s44160-024-00518-4.

28. T. Wang, J. Hu, R. Ouyang, et al., "Nature of Metal-Support Interaction for Metal Catalysts on Oxide Supports," *Science* 386 (2024): 915–920, https://doi.org/10.1126/science.adp6034.

29. Q. Liu, Q. Zhang, W. Shi, H. Hu, J. Zhuang, and X. Wang, "Self-Assembly of Polyoxometalate Clusters Into Two-Dimensional Cluster-phene Structures Featuring Hexagonal Pores," *Nature Chemistry* 14 (2022): 433–440, https://doi.org/10.1038/s41557-022-00889-1.

30. Y. Guo, R. Zhang, S. Zhang, et al., "Steering sp -Carbon Content in Graphdiynes for Enhanced Two-Electron Oxygen Reduction to Hydrogen Peroxide," *Angewandte Chemie International Edition* 63 (2024): e202401501, https://doi.org/10.1002/anie.202401501.

31. L.-L. Ling, L. Jiao, X. Liu, et al., "Potassium-Assisted Fabrication of Intrinsic Defects in Porous Carbons for Electrocatalytic CO_2 Reduction," *Advanced Materials* 34 (2022): 2205933, https://doi.org/10.1002/adma.202205933.

Supporting Information

Additional supporting information can be found online in the Supporting Information section.

Supporting File 1: anie72155-sup-0001-SuppMat.docx.

Supporting File 2: anie72155-sup-0002-Movie S1. Ru clusterrene.mp4.

Supporting File 3: anie72155-sup-0003-Movie S2. Ru nanoparticle.mp4.

Supporting File 4: anie72155-sup-0004-Supplementary movies.docx.